Effects of point cloud density, interpolation method and grid size on derived Digital Terrain Model accuracy at micro topography level

F. Agüera-Vega , M. Agüera-Puntas , P. Martínez-Carricondo , F. Mancini & F. Carvajal

Published online: 18 Jun 2020.

Submit your article to this journal

View related articles

View Crossmark data

Taylor & Francis
Taylor & Francis Group

Check for updates

Effects of point cloud density, interpolation method and grid size on derived Digital Terrain Model accuracy at micro topography level

F. Agüera-Vega [iD][a], M. Agüera-Puntas[a], P. Martínez-Carricondo [iD][a], F. Mancini[b] and F. Carvajal [iD][a]

[a]Department of Egineering, University of Almería (Agrifood Campus of International Excellence, ceiA3), Mediterranean Research Center of Economics and Sustainable Development (CIMEDES), Almería, Spain; [b]Department of Engineering "Enzo Ferrari", University of Modena and Reggio Emilia, Modena, Italy

ABSTRACT

The objective of this study was to evaluate the effects of the three dimensional (3D) point cloud density derived from Unmanned Aerial Vehicle (UAV) photogrammetry (using Structure from Motion (SfM) and Multi-View Stereopsis (MVS) techniques), the interpolation method for generating a digital terrain model (DTM), and the resolution (grid size (GS)) of the derived DTM on the accuracy of estimated heights in small areas, where a very accurate high spatial resolution is required. A UAV-photogrammetry project was carried out on 13 m × 13 m bare soil with a rotatory wing UAV at 10 m flight altitude (equivalent ground sample distance = 0.4 cm), and the 3D point cloud was derived. A stratified random sample (200 points in each square metre) was extracted and from the rest of the cloud, 15 stratified random samples representing 1, 2, 3, 4, 5, 10, 15, 20, 30, 40, 50, 60, 70, 80, and 90% were extracted. Five replications of each percentage were extracted to analyse the effect of cloud density on DTM accuracy. For each of these 15 × 5 = 75 samples, DTMs were derived using four different interpolation methods (Inverse Distance Weighted (IDW), Multiquadric Radial Basis Function (MRBF), Kriging (KR), and Triangulation with Linear Interpolation (TLI)) and 15 DTM GS values (20, 15, 10, 9, 8, 7, 6, 5, 4, 3, 2, 1, 0.67, 0.50, and 0.40 cm). Then, 75 × 4 × 15 = 4500 DTMs were analysed. The results showed an optimal GS value for each interpolation method and each density (most of the cases were equal to 1 cm) for which the Root Mean Square Error (RMSE) was the minimum. IDW was the interpolator that yielded the best accuracies for all combinations of densities and GS. Its RMSE when considering the raw cloud was 1.054 cm and increased by 3% when a point cloud with 80% extracted from the raw cloud was used to generate the DTM. When the point cloud included 40% of the raw cloud, RMSE increased by 5%. For densities lower than 15%, RMSE increased exponentially (45% for 1% of raw cloud). The GS minimizing RMSE for densities of 20% or higher was 1 cm, which represents 2.5 times the ground sample distance of the pictures used for developing the photogrammetry project.

CONTACT F. Agüera-Vega ✉ faguera@ual.es 🔲 Department of Egineering, University of Almería (Agrifood Campus of International Excellence, ceiA3), Mediterranean Research Center of Economics and Sustainable Development (CIMEDES), Almería C.P. 04120, Spain

1. Introduction

A Digital Elevation Model (DEM) is a mathematical representation of an object and is often used for describing terrains and their elevations. It plays an important role in applications related to terrain modelling, hydrological modelling, or landscape evolution due to the erosion process (Mancini et al. 2013; Asal 2016; Jaud et al. 2016; Schwendel and Milan 2019).

Furthermore, Unmanned Aerial Vehicles (UAVs) can collect data that combined with remote sensing techniques, provide three dimensional (3D) models and orthophotographs with a high spatial and temporal resolution (Jaud et al. 2016). These products are very useful for landscape monitoring, e.g. reconstruction of extreme topography (Agüera-Vega et al. 2018), precision agriculture (Martinez-Guanter et al. 2019; Campos et al. 2019; Agüera Vega et al. 2015), landslide monitoring (Rossi et al. 2018), and erosion assessment (Gong et al. 2019; Eltner et al. 2015; Castillo et al. 2012; Momm et al. 2013).

The integration of photogrammetry and computer vision has provided the Structure from Motion (SfM) technique, which makes it possible to collect images from different heights and in different directions with greater flexibility and high quality results (Atkinson 1996; Hartley and Zisserman 2003). SfM automatically solves the geometry of the scene and the camera positions and orientation without the need to specify a priori a network of targets that have known 3D positions (Snavely, Seitz, and Szeliski 2008; Westoby et al. 2012; Vasuki et al. 2014). The Multi-View Stereopsis (MVS) technique has been incorporated into SfM, which allows the 3D structure to be derived from overlapping photography acquired from multiples angles. Furthermore, the Scale Invariant Feature Transform (SIFT) operator has been shown to be one of the most robust for key-point detection for generating 3D point clouds from two dimensional (2D) photographs (Remondino and El-Hakim 2006; Juan and Gwun 2009). All this has led to the so-called UAV-photogrammetry, which consists of taking pictures from a non-metric camera mounted on a UAV to obtain a 3D point cloud representing the studied object.

The extraction of precise and reliable 3D metric information from images requires accurate camera calibration procedure (Luhmann, Fraser, and Maas 2016; Remondino and Fraser 2006). Camera calibration is the determination of internal geometry of a camera. Furthermore, the most commonly sensor used in UAV-photogrammetry are consumer digital cameras (Carrivick, Smith, and Quincey 2016) and these have unstable and fluctuating internal geometry (Nex and Remondino 2014). Since there is not easy solution to estimate the parameters that define this geometry, several proposals have been studied (e.g. Pérez, Agüera, and Carvajal 2013; Gašparovic and Gajski 2016). Remondino and Fraser (2006) proposed a calibration methods classification according to the parameter estimation and optimization technique employed: linear techniques, non-linear techniques, and a combination of both of these techniques. With SfM approaches, calibration can be carried out using a large number of tie points, which provide redundancy in the solution, and can yield a high internal precision, but it can mask deficiencies in the external accuracy and reliability (Nesbit and Hugenholtz 2019; Luhmann, Fraser, and Maas 2016). Nevertheless, following well-proven rules for self-calibration an accurate self-calibration, observation errors can be minimized, providing in this way more accurate estimates of calibration parameters, enabling accurate and reliable measurements from practically any camera (Remondino and Fraser 2006).

Given a 3D point cloud, several factors affect the accuracy of the DEM, such as the density and distribution of the point cloud, grid resolution, and the interpolation method used to generate the DEM. UAV-photogrammetry is able to generate high 3D point densities, however, this must be accompanied by the proper system for data storage, data processing, and manipulation of large volumes of data. High 3D point densities and high DEM grid resolution imply long processing time both in point cloud generation and DEM generation. Therefore, reductions of such high point densities help reduce the cost of data acquisition and data computation (Singh et al. 2015). Although reduction in point cloud densities and DEM grid size (GS) reduction are expected to have direct effects on DEM characteristics, if those effects are not significant for a given application, this could result in saving in data acquisition and processing costs by a balance between them.

Although there are no published works studying these effects on data generated from UAV-photogrammetry, there are some on a 3D cloud point generated with terrestrial Light Detection and Ranging (LiDAR) technology. For example, Anderson, Thompson, and Austin (2005) reduced the original LiDAR point cloud, resulting in datasets with 50%, 25%, 10%, 5%, and 1% of their original densities. Furthermore, they used two interpolators (Inverse Distance Weighted (IDW) and ordinary Kriging (KR)) to generate the DEM. A study of the errors concluded that LiDAR datasets could withstand substantial data reductions and maintain adequate accuracy for elevation predictions and that simple interpolation approaches such as IDW could be sufficient for generating the DEM.

Similarly, Liu et al. (2007) explored the effect of point cloud density acquired with LiDAR and examined the scope for data volume reduction without affecting the efficiency in data storage and processing. They concluded that although datasets could be reduced to increase the efficiency of DEM generation, the maximum level of data reduction depends on the original data density, interpolation method, DEM GS, and terrain characteristics. Liu and Zhang (2008) then explored the effects of LiDAR data density on the accuracy of DEMs and examined how much a set of this data could be reduced while maintaining adequate accuracy for DEM generation. They concluded that data reduction mitigates the data redundancy and improves data processing efficiency in terms of both storage and processing time.

For a large area, Singh et al. (2015) evaluated the effects of LiDAR point cloud density on the biomass estimation of remnant forest in a rapidly urbanizing region and concluded that data with an average point spacing of 0.70 to 1.50 m could result in cost-effective acquisition and data processing. Furthermore, Asal (2016) evaluated the effects of reduction in airborne LiDAR data on the visual and statistical characteristics of the created DEM and concluded that the DEM accuracy decreased by only 4.83% when the point cloud was reduced by 50%.

All the above related works were developed for large areas, but there are occasions that require the study of smaller areas with a high level of detail and the required scale for representing these is therefore greater than that required for representing larger areas. In this sense, Asensio et al. (2019) developed a methodology based on a wind tunnel and a 3D laser scanner to estimate wind erosion, relating the change in microrelief to soil loss. They worked on 120 cm2 microplots with 2.98×10^6 3D points scanned in each studied plot. Then, two 0.1 cm $\times$ 0.1 cm resolution Digital Terrain Models (DTMs), one before and one after wind simulation, were generated and compared to estimate soil loss. The interpolation method to obtain the DTMs was not indicated.

Similarly, Schmid, Schack-Kirchner, and Hildebrand (2014) used a high-resolution terrestrial laser scanner to assess erosion risk due to mechanized logging with crawler harvesters on steep slopes. The plots studied were 20 m2 and were scanned before and after the logging operation and after one year of exposure to rain. The surface roughness was estimated from DTMs with resolutions of 0.5 mm × 0.5 mm and 1 cm × 1 cm. The interpolation method was not mentioned. One conclusion of this work was that the roughness index calculated was influenced by DTM resolution.

García-Serrana, Gulliver, and Nieber (2018) formulated the relevance of the fractal approach for understanding the relationship of surface roughness to overland flow patterns. The system used to generate the 3D point cloud was based on close-range photogrammetry and the DTM was generated with 0.1 cm × 0.1 cm resolution. No indications about the interpolation method used to generate the DTM were given. The study of Smith and Warburton (2018) used SfM surveys to examine its ability to represent the fine details and to quantify roughness for different peat surfaces. To realize these objectives, they derived two DTMs, one at 0.1 cm × 0.1 cm resolution and one at 0.5 cm × 0.5 cm resolution. The interpolation method used was not mentioned.

In view of all these mentioned works, it can be stated that both LiDAR and SfM techniques generate high-density 3D point clouds and that it would be interesting to study the relationship between data density reduction and the accuracy of the generated DEM. The objective of this study is therefore to evaluate the effects of 3D point cloud density derived from UAV-photogrammetry and SfM and MVS techniques, the interpolation method used to generate the DEM, and the resolution (GS) of the derived DEM on the accuracy of the estimated heights in small areas, where a very high spatial resolution and accuracy are required.

2. Materials and methods

2.1. Study site

The study site was located in Tabernas Desert (Almería), Southeast Spain. The south-west and north-east coordinates UTM (Zone 30, European Terrestrial Reference System 89 (ETRS89)) of this area are (548948, 4096735) and (548961, 4096748), respectively. It is a square 13 m × 13 m in size that covers an area of 169 m2. The selection of this area was based on its morphology, which includes a wide range of variability. Furthermore, the terrain is free of vegetation, meaning there was no difference between the Digital Surface Model (DSM), the DTM, and the DEM. The elevation range was 4.8 m. Figure 1 represents the location of the study site and an orthophoto and contour map of the study site.

2.2. Image collection

The images used in this work were taken from a rotatory wing DJI Mavic Air with four rotors. Its weight is 430 g, and it is equipped with a navigation system using GPS and GLONASS. In addition, it is equipped with a front, rear, and lower vision system that allows it to detect surfaces with a defined pattern and adequate lighting and avoid obstacles within a range between 0.5 m and 10 m. Furthermore, the UAV is equipped with a Red
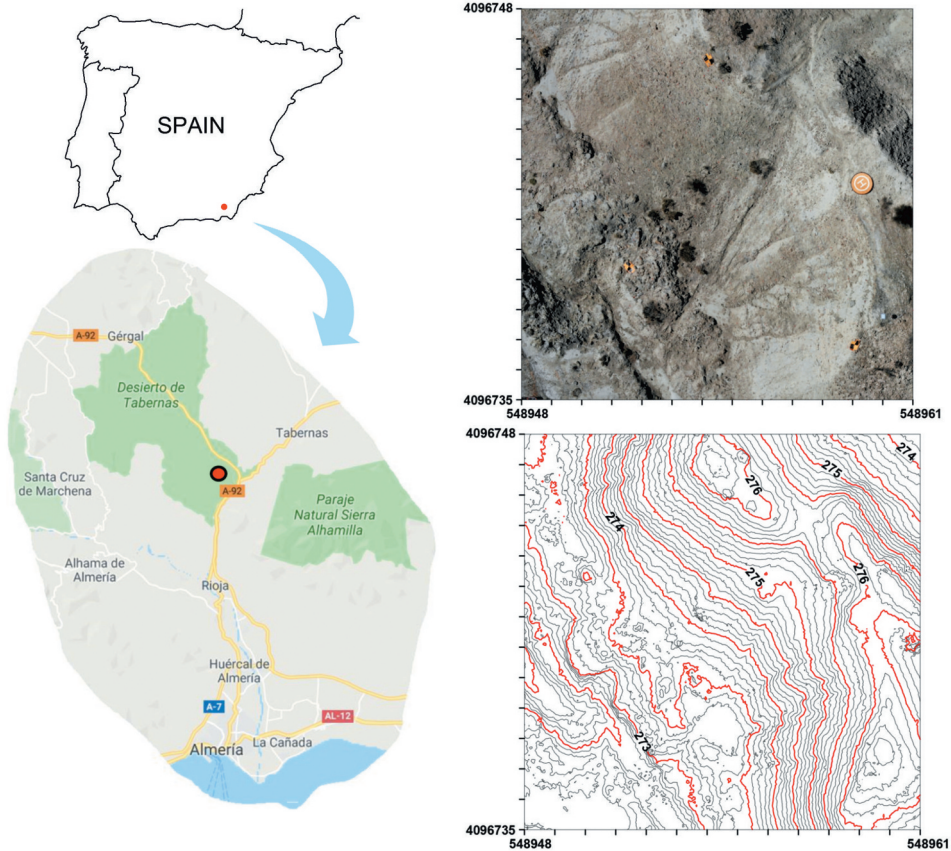
Figure 1. Location of the study area (red points in the figures on the left), orthophoto (top right), and contour map (bottom right). Coordinates are UTM (zone 30, ETRS89).

Green Blue (RGB) camera with a 1/2.3" Complementary Metal Oxide Semiconductor (CMOS) sensor, f/2.8 aperture, and 12 megapixels (4056 × 3040) mounted on a motion-compensated three-axis gimbal. The lens has a fixed focal length of 24 mm (equivalent to the 35 mm format) and a horizontal Fiel Of View (FOV) of 85°.

The flight was carried out with an autopilot using the UgCS software (UgCS 2019), which allows a flight altitude fitted parallel to the ground to be configured by introducing a DSM of the study site. In this way, there was no scale difference between photographs. This DSM was generated previously in the same field visit through a photogrammetric project that was processed on site. Flight altitude was set at a constant distance of 10 m, which yielded a ground sample distance (GSD) of 0.46 cm. The forward and side overlaps were 85% and 65%, respectively.

Furthermore, the coordinates of four Ground Control Points (GCPs) placed on the corners of the study area and marked with targets that were A3 format in size (297 × 420 mm) were measured with the Global Navigation Satellite System (GNSS). This was done by working with differential corrections in real-time kinematic (RTK) mode, with the base station on a geodesic pillar located within 1 km of the studied site. Both the rover and base GNSS receivers were Trimble R6 units. With this configuration, the maximum

horizontal and vertical Root Mean Square Error (RMSE) were ±9 and ±16 mm, respectively. Regardless, the purpose of this task was to get high accuracy in the georeference of the DSM, not to check its accuracy.

2.3. Photogrammetric processing

The photogrammetric project was processed using Pix4Dmapper Pro version 3.1.23 (Pix4Dmapper 2019), a software application based on the SfM and MVS techniques mentioned in the introduction section. This software was set to obtain the highest 3D point cloud density and quality by adjusting the following processing options in the Point Cloud Densification box: Image Scale, which defines the scale of the images at which additional 3D points are computed was fixed to 1 and the Multiscale option was selected; Point Density, which defines the density of the densified point cloud was fixed to high, the maximum level; and the Minimum Number of Matches, which represents the minimum number of valid re-projections of this 3D point to the images was fixed to 6 to produce a point cloud with high quality.

Eighteen images were taken on 8 March 2019 and were checked to ensure no blurred images were included in the project. None of these images was discarded. Processinng included self-calibrating bundle block using camera internal orientation parameters: focal length, principal point, and lens distortion terms, consisting in three radial (R1, R2 and R3), and two tangential (T1 and T2) and camera external orientation paramenters, consisting in location coordinates and orientation (roll, pitch, yaw). Camera calibration was carried out using non-linear techniques, starting from a set of parameters given for the camera manufacturer. This method provides a rigorous and accurate modelling of the camera internal orientation and lens distortion parameters through an iterative least-squares estimation process (Brown 1971). In this way, the calculated parameters were: f = 5.549 mm, principal point X coordinate = 3.025 mm, principal point Y coordinate = 2.246 mm, R1 = 0.242, R2 = −0.763, R3 = 0.609, T1 = 0.001 and T2 = 0.000034. Location coordinates and orientation all the images were loaded from the Exchangeable image file format (Exif) data.

Identification of the GCPs in the images was carried out visually using an incorporated tool in the processing software for assigning the absolute geolocation of the photogrammetric block. Each of these four GCPs was in at least 10 photographs and the projection error (average distance in the images where each GCP had been marked and where it had been reprojected) ranged from 0.315 to 0.803 pixels. The product obtained from the photogrammetric project used in this study was the 3D point cloud.

2.4. 3D point cloud processing

To study the influence of the 3D point cloud density, the interpolation method, and the GS of the derived DSM on the accuracy of the DSM, a factorial experimental design was carried out. Figure 2 shows the flowchart of the procedure followed in this study. The whole procedure described in this section was programmed using Golden Software ScripterTM, which works with the Surfer 8.01 (Golden Software 2019) modelisation engine via instructions written in a Visual Basic-like programming language.
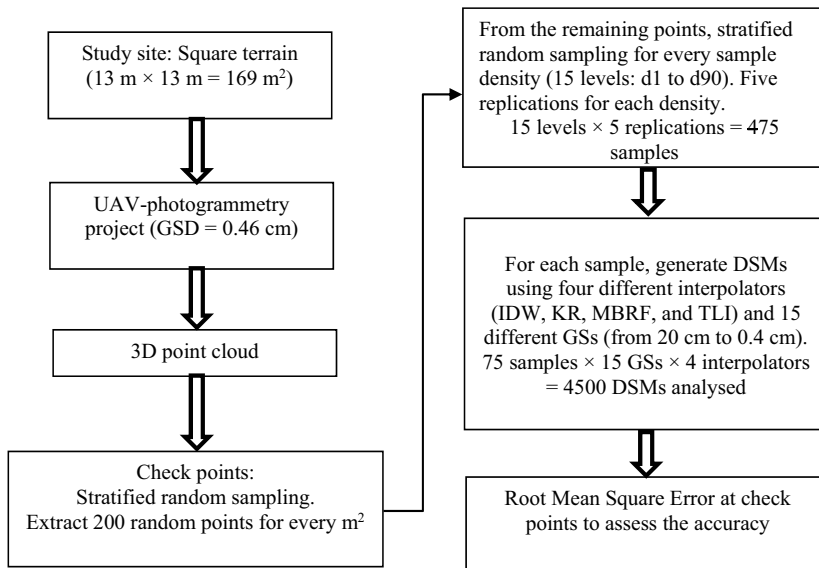
Figure 2. Flowchart of the procedure followed in this study.

2.4.1. Datasets

Considering the objectives proposed in this work, the errors inherent in the coordinates of the 3D points generated in the photogrammetric project have been considered null. Obviously, the point cloud has an inherent error, but we studied only the error inherent to the interpolator used to generate the DSM from the point cloud. In this work, we use SfM only to have a point cloud with characteristics (density and distribution) associated to this thecnique. From the initial 3D point cloud, a random sample of 200 Check Points (CPs) were extracted for every square metre of the study site. Therefore, a total of $200 \times 13 \times 13 = 33800$ CPs were used to evaluate the derived DSM accuracy. Furthermore, 15 stratified random samples with different numbers of points were extracted from the remaining points, with five repetitions per sampling density. The sampling densities were those corresponding to 1, 2, 3, 4, 5, 10, 15, 20, 30, 40, 50, 60, 70, 80, and 90% of the total number of 3D points in the generated cloud, which were named as d1, d2, d3, d4, d5, d10, d15, d20, d30, d40, d5, d60, d70, d80, and d90, respectively. The raw point cloud was named d100. These $5 \times 15 = 75$ files were extracted from the raw 3D point cloud using an informatics program developed by the authors in Visual Basic v6.0 language.

2.4.2. Interpolation methods

The interpolation methods evaluated in this work are Inverse Distance Weighted (IDW), Multiquadric Radial Basis Function (MRBF), Kriging (KR), and Triangulation with Linear Interpolation (TLI), which are all incorporated in the above-mentioned software Surfer 8.01. For each of the 75 extracted files and for each of the interpolation methods, the DSM GS was set at 15 different values: 20, 15, 10, 9, 8, 7, 6, 5, 4, 3, 2, 1, 0.67, 0.50, and 0.40 cm. Then, $75 \times 15 \times 4 = 4500$ DSMs were analysed.

2.4.2.1. Inverse distance weighted. This is a weighted average interpolator and one of the most used for surface modelling. It is based on the idea that the influence of one point relative to another declines with the distance from the grid node, where the value is interpolated. The weighting factor assigned to each data point determines the rate at which this influence decreases as the distance increases. It is an exact and local interpolator that uses the Equation (1) to estimate the value for a non-sampling point (X, Y):

$$Z_j^{Estimated} = \frac{\sum_{i=1}^{i=m_j} \frac{Z_i}{d_{i,j}^{\beta}}}{\sum_{i=1}^{i=m_j} \frac{1}{d_{i,j}^{\beta}}}, \tag{1}$$

where $Z_j^{Estimated}$ is the interpolated height in the *jth* DSM node, Z_i ($i = 1, 2, \ldots, m_j$) is the *ith* point height of the cloud used to interpolate the *jth* DSM node, $d_{i,j}$ is the distance between the *jth* DSM node and the *ith* point of the cloud used to interpolate the *jth* DSM node, m_j is the number of points of the cloud used to interpolate the *jth* DSM node, and β is the weighting power. In this study $\beta = 2$.

2.4.2.2. Radial basis function. This exact interpolator includes a diverse group of interpolation methods that use a basic equation dependent on the distance between the interpolated point and the sampling points (Carlson and Foley 1992). Its expression that is generally used to interpolate topographic surfaces is given in Equation (2).

$$Z_j^{Estimated} = \sum_{i=1}^{i=m_j} a_i \Psi(r_{i,j}), \tag{2}$$

where $Z_j^{Estimated}$ is the interpolated height in the *jth* DSM node, $\Psi(r_{i,j})$ represents the radial basis functions, $r_{i,j}$ is the distance between the *jth* DSM node and the *ith* point of the cloud used to interpolate the *jth* DSM node, a_i are scalar values (called weights) assigned to each point of the cloud used to interpolate the *jth* DSM node, and m_j is the number of points of the cloud used to interpolate the *jth* DSM node.

To calculate the scalar values a_i, it is necessary to solve the linear system **M × A = Z**, where M is an m_j-order square matrix containing the distances between the DSM node and the points used to interpolate this node, **A** is a vector containing the a_i values that have to be calculated, and **Z** is a vector containing the height of each point used to interpolate this node.

In terms of the ability to fit the data and to produce a smooth surface, the Multiquadric method is considered by many authors the best of all the radial basis function methods (Franke 1982; Powell 1990). In the MRBF, the radial basis functions take the form exposed in Equation (3).

$$\Psi(r) = \sqrt{r^2 + c^2}, \tag{3}$$

where r is the distance from the node to the point of the cloud and c is the smoothing factor. There is no universal method to calculate this factor and several authors have proposed different formulas (e.g. Carlson and Foley (1991)). In this study, the Equation (4) is used (Golden Software 2019):

$$c^2 = \frac{D^2}{25 \times n}, \tag{4}$$

where D is the length of the diagonal of the data extent and n is the number of data points.

2.4.2.3. Kriging. This is a geostatistical interpolation method that has demonstrated good behaviour in many fields. It attempts to express the trends suggested in a data sample (3D point cloud), which means, for example, that high points might be connected along a ridge rather than isolated by bullseye type contours. The general expression for Ordinary Kriging is given in Equation (5).

$$Z_j^{Estimated} = \sum_{i=1}^{i=m_j} \lambda_i Z_i \tag{5}$$

where $Z_j^{Estimated}$ is the interpolated height in the jth DSM node, Z_i ($i = 1, 2, ..., m_j$) is the ith point height of the cloud used to interpolate the *jth* DSM node, and λ_i is the weight assigned to each point of the cloud used to interpolate the *jth* DSM node. These values should be set so that the estimator is unbiased ($\sum_{i=1}^{i=m_j} \lambda_i = 1$) and the variance is minimal. m_j is the number of points of the cloud used to interpolate the *jth* DSM node.

2.4.2.4. Triangulation with linear interpolation. This is an exact interpolator that uses the optimal Delaunay triangulation (Lee and Schachter 1980), creating triangles by drawing lines between data points in such a way that no triangle edges are intersected by other triangles. In this way, the entire studied surface will be covered by a 3D triangle net and the height estimation at a given grid node is made by linear interpolation considering the triangle that covers that node.

2.4.3. Evaluation of DEM accuracy
As mentioned in Section 2.4.1, 33800 points were extracted from the raw 3D point cloud to check the accuracy of the extracted elevations from the DSMs created from reduced point data densities. The measure used to evaluate the performance of the DSMs was the RMSE (Yang and Hodler 2000), calculated with Equation (6).

$$RMSE = \sqrt{\frac{\sum_{i=1}^{i=n} \left(Z_i^{Estimated} - Z_i^{Real}\right)^2}{n}}, \tag{6}$$

where Z_i^{Real} is the elevation of the ith ($i = 1, 2, 3, ..., 33800$) CP extracted from the 3D point cloud, $Z_i^{Estimated}$ is the elevation estimated for the$i$th CP in the DSM under study, and n is the number of CPs (33800). For each CP, its estimated Z was calculated from the derived raster grid considering its X and Y coordinates. A set of five RMSE values corresponding to each replication was calculated for each combination of the 3D point cloud density, DSM GS, and interpolator. Analysis of variance (ANOVA) of the designed factorial model was carried out by taking the RMSE as the dependent variable and the interpolation method and sampling density as the independent variables.

3. Results

The raw 3D point cloud derived from the photogrammetric project yielded 10516447 points, which corresponds to 62227 points m^{-2} Table 1 shows the correspondence between the studied percentages of points extracted from the raw point cloud, the number of points, the point cloud density or number of points per square metre, and the square GS of a DSM that has as many nodes as points extracted from the raw cloud (equivalent square GS), which ranged from 4.01 cm to 0.4 cm. The number of points per square metre ranged from 622 to 62227. From here, the percentage of the extracted points will be referred to as density as they are directly related.

Figure 3 shows the relationship between the DSM GS and the RMSE (average of five repetitions) for each point cloud density studied. To clarify this figure, the logarithmic scale was used in both axes. As can be observed in this figure, all curves show a similar shape: as the GS decreases, the RMSE also decreases until reaching a certain GS value (which was not the same in all cases but was close to 1 cm), from which the RMSE then increases. Moreover, for the four interpolation methods, the curves are ordered by density, meaning that for a given interpolator the curve corresponding to a certain density was below that corresponding to a lower density. For a given interpolation method, the differences in RMSE between different densities were lower at the extremes and higher in the central zone, which is precisely where the minimum RMSE values were found. This means that the influence of point density on the RMSE for large and small GS values was not as noticeable as when the GS values were close to or somewhat greater than the optimum.

Table 2 shows the minimum RMSE (average of the five replications) and the GS that was reached for each interpolator and 3D point cloud density studied. For a given RMSE column, values with the same letter are not statistically different (p < 0.05).

In view of this table, it can be stated that for densities equal or greater than d20, the minimum RMSE has been reached for a GS equal to 1 cm for all interpolation methods. For densities lower than d20, the optimum GS varied depending on the interpolation method used and up to d2, the highest optimum GS was 3 cm. For the lowest point density studied, d1, the optimal GS values were different for each interpolation method: 10, 4, 6, and 3 cm for IDW, KR, MRBF, and TLI, respectively. The ANOVA and least significant difference tests showed that when considering each interpolation method separately, the RMSE values were grouped into statistically different sets (p < 0.05). These differences were most clearly shown for the IDW and KR methods, where there were no overlaps between the sets. For the MRBF and TLI, the value sets were not as well defined as for the other interpolators. RMSE values corresponding to d80 and d90 form a homogeneous group for all interpolation methods (MRBF and TLI overlap with other groups of values).

Figure 4 shows the data presented in Table 2. The curves representing the minimum RMSE reached for each 3D point cloud density and each interpolation method show an asymptotic tendency as the point density increases towards the RMSE corresponding to d100. It can also be seen that the curve corresponding to the MRBF method is the one that is most separated from the rest.

After studying these results, two groups in each interpolation method were considered: one including the RMSEs of d40 and the other including those of d80. The ANOVA showed statistical differences (p < 0.05) between interpolation methods in both groups.

Table 1. Correspondence between the studied percentages of points extracted from the raw point cloud, the number of points, the number of points per square metre, and the square GS of a DSM that has as many nodes as points extracted from the raw cloud (equivalent square GS).

| Percentage (%)	1	2	3	4	5	10	15	20
Number of points	105164	210329	315493	420658	525822	1051645	1577467	2103289
Number of points $\times$ m^{-2}	622	1245	1867	2489	3111	6223	9334	12445
Equivalent square GS (cm)	4.01	2.84	2.31	2.00	1.79	1.27	1.04	0.90
Percentage (%)	30	40	50	60	70	80	90	100
Number of points	3154934	420,579	5258224	6309868	7361513	8413158	9464802	10516447
Number of points $\times$ m^{-2}	18668	24891	31114	37336	43559	49782	56005	62227
Equivalent square GS (cm)	0.73	0.63	0.57	0.52	0.48	0.45	0.42	0.40
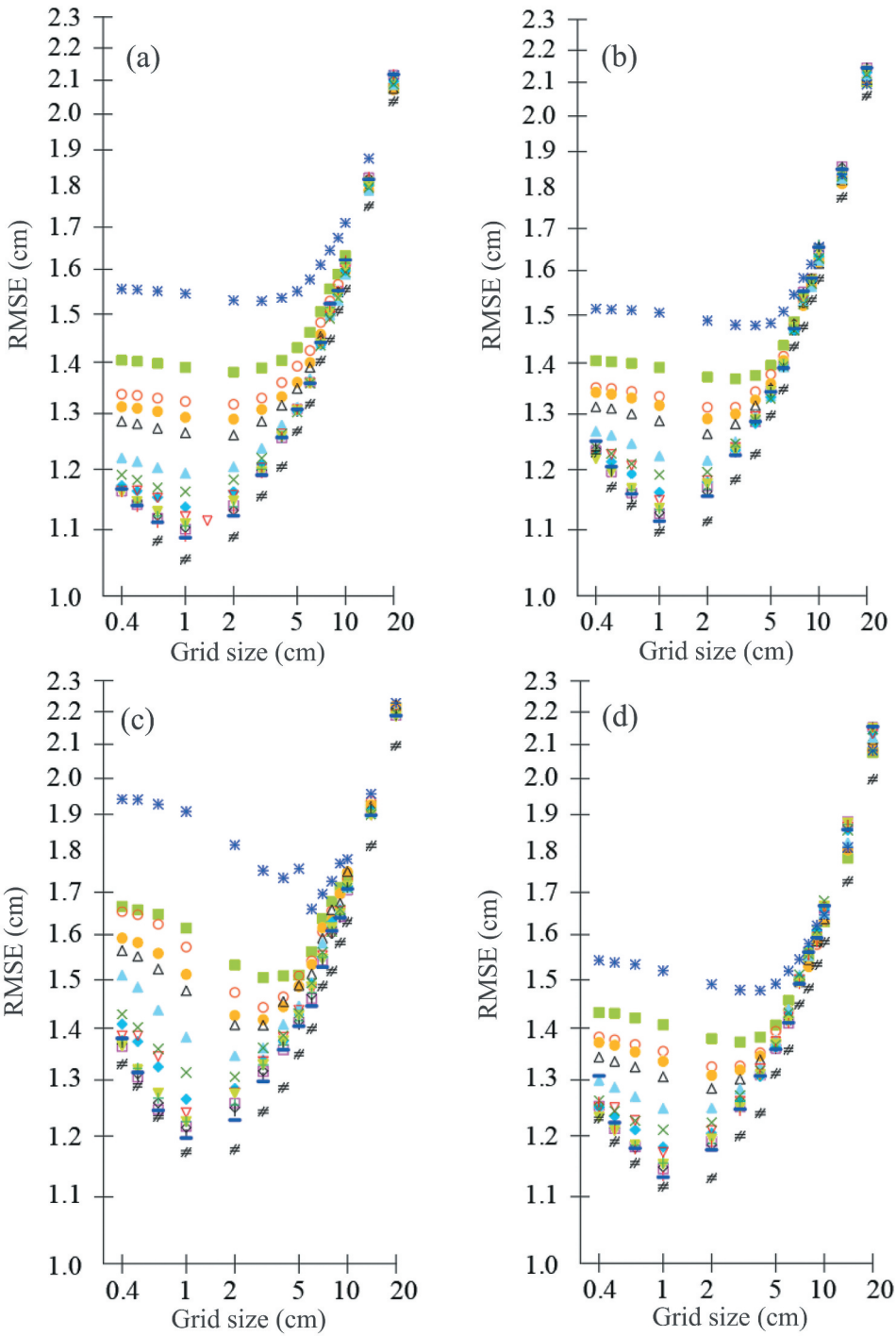
Figure 3. RMSE (*y*-axes, cm) for each GS (*x*-axes, cm), interpolation method, and point cloud density. Interpolation method: (a) IDW; (b) KR; (c) MRBF; (d) TLI. Point cloud density: * d1; ■ d2; ○ d3; ● d4; Δ d5; ▲ d10; ×d15; ♦ d20; d30; ▼ d40; + d50; ◊ d60; □ d70; | d80; — d90; and # d100. To clarify this figure, the logarithmic scale was used in both axes.

Table 2. The minimum RMSE (cm) and the GS for which it was found (optimum GS, cm) for each interpolator and 3D point cloud density studied. RMSE values are the average of the five replications. In each RMSE column, values with the same letter are not statistically different. The last row shows data corresponding to the raw 3D point cloud.

Density (%)	IDW		KR		MRBF		TLI	
	Opt. GS	RMSE	Opt. GS	RMSE	Opt. GS	RMSE	Opt. GS	RMSE
d1	10	1.529[a]	4	1.478[a]	6	1.660[a]	3	1.477[a]
d2	2	1.380[b]	3	1.368[b]	3	1.505[b]	3	1.372[b]
d3	2	1.318[c]	2	1.313[c]	3	1.442[c]	2	1.325[c]
d4	2	1.290[d]	2	1.291[d]	3	1.417[c,d]	2	1.309[d]
d5	2	1.260[e]	2	1.263[e]	3	1.406[d]	2	1.284[e]
d10	1	1.193[f]	2	1.216[f]	2	1.346[e]	1	1.248[f]
d15	1	1.162[g]	1	1.191[g]	2	1.306[f]	1	1.210[g]
d20	1	1.136[h]	1	1.161[h]	1	1.265[g]	1	1.181[h]
d30	1	1.121[i]	1	1.148[i]	1	1.241[g,h]	1	1.172[h]
d40	1	1.110[j]	1	1.135[j]	1	1.225[h,i]	1	1.152[i]
d50	1	1.106[j]	1	1.132[j]	1	1.225[h,i]	1	1.154[i]
d60	1	1.103[j]	1	1.127[j]	1	1.215[h,i]	1	1.148[i]
d70	1	1.101[j]	1	1.126[j]	1	1.217[h,i]	1	1.145[i,j]
d80	1	1.089[k]	1	1.114[k]	1	1.203[i]	1	1.133[j]
d90	1	1.088[k]	1	1.114[k]	1	1.197[i]	1	1.131[j]
d100	**1**	**1.054**	**1**	**1.097**	**1**	**1.173**	**1**	**1.116**
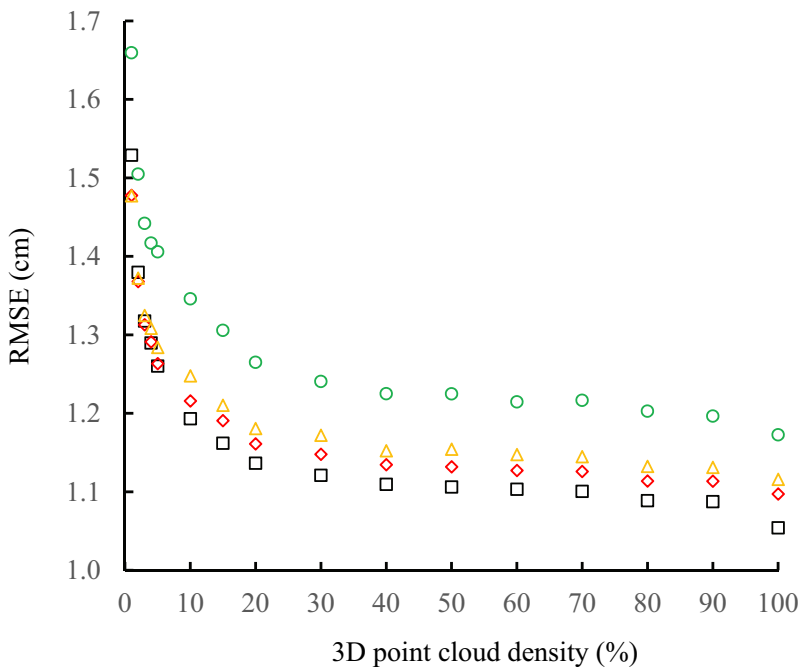
Figure 4. Minimum RMSE reached for each interpolator (□ IDW; ◊ KR; ○ MRBF; Δ TLI) vs. 3D point cloud density studied. RMSE values are the average of the five replications.

4. Discussion

UAV-derived 3D point clouds provide a new strategy for monitoring terrain surfaces with an extremely high level of spatial and temporal resolution. These clouds were used to derive DSMs, which provide a very useful basis for carrying out calculus related to terrain

monitoring. In the literature, virtually all work studying the accuracy of the DSMs generated from data acquired with SfM and MVS techniques does not separate the error due to the 3D point cloud generation process from the interpolation method used to generate the DSM, the fixed GS, or the number of points in the point cloud.

All curves shown in Figure 3 (RMSE vs. GS, for all interpolation methods and densities studied) have a minimum RMSE value reached for a certain GS and values smaller than these yield a worse RMSE. This indicates that the generated DSM does not fit as well as those generated with a bigger GS. Although there are works in which the relationships between the optimal GS and other factors, such as the point cloud density, terrain morphology, and others have been established (e.g. Hengl (2006)), all of them were carried out on larger areas and point densities lower than those considered in this work. Table 2 indicates that the GS for which the minimum RMSE was reached for each interpolator and each density was not related to the 3D point cloud density or to the interpolation method. From d100 to d20, the optimum GS was 1 cm. For values lower than d20, the optimum GSs adopt different values but are not related to density or the interpolator.

For all the studied interpolation methods, data density was related to DSM accuracy: RMSE increased as data density decreased. This is because as the distance between the sample points increased, the accuracy of the generated DSM decreased (Anderson, Thompson, and Austin 2005). Anderson, Thompson, and Austin (2005) studied a set of six reduced 3D point clouds derived from a series of 10 100-ha LiDAR-tiled study sites. Point densities ranged from 181.03 points m^{-2} (no reduced point cloud) to 1.80 points m^{-2} (1% of raw cloud). Furthermore, they used two interpolation methods: IDW and KR. For the IDW interpolator, the results showed an increase of RMSE from density equal to 100% (17.31 cm) to density equal to 1% (35.66 cm). Then, the increase represented 106% of the minimum RMSE. For the KR interpolator, an increase from 0.01% (34.24 cm) to 1% (17.25 cm) represented 98.5% of the minimum RMSE.

Liu et al. (2007) found similar results using the IDW interpolator on a set of six reduced 3D point clouds derived from a raw LiDAR cloud. They studied densities from 0.037 points m^{-2} (no reduced point cloud) to less than 0.001 points m^{-2} (1% of raw cloud) in a study area of 113 km^2. An increase of RMSE from 100% (18.4 cm) to 1% of the 3D point cloud (64.1 cm) represented 248% with respect to the minimum RMSE.

The study site of the present work was 169 m^2 in area and the point densities ranged from 62227 points m^{-2} (no reduced point cloud) to 622 points m^{-2} (1% of raw cloud) (Table 1). This study, as opposed to those cited above, was looking for highly accurate and detailed microscale topography and therefore the point densities should be higher than those used in the cited works.

Considering the minimum and maximum RMSEs found for each interpolation method (Table 2), the increases represented 45% for IDW (from 1.529 to 1.054 cm), 35% for KR (from 1.478 to 1.097 cm), 42% for MRBF (from 1.660 to 1.173 cm), and 32% for TLI (from 1.477 to 1.116 cm). All these increases were lower than those reported by Anderson, Thompson, and Austin (2005) and Liu et al. (2007). Nevertheless, Asal (2016) reported an increase of RMSE of approximately 260% when the point cloud was reduced to 6%.

For each density value studied, the RMSE values derived from the four interpolators were ordered from highest to lowest as follows: IDW, KR, TLI, and RBF. Although the differences between the RMSEs derived from the IDW, KR, and TLI interpolators were not

very large, the classical method of IDW clearly proved to be more appropriate than the others, which agrees with some of the developers of UAV-photogrammetric software (Metashape 2019; Pix4Dmapper 2019) who have used this interpolation method to generate DSMs. Nevertheless, Anderson, Thompson, and Austin (2005) reported no discernible difference in RMSE between IDW and KR and a similar conclusion was derived from the results of Lloyd and Atkinson (2002).

Within each interpolation method, the least significant difference test carried out on the RMSE showed d80 and d90 to be homogeneous groups (p < 0.05), another homogeneous group from d40 to d70, and densities from d30 to d1 are homogeneous groups themselves. All these homogeneous groups were clearly defined for IDW and KR. For TLI, the groups were a bit more diffuse, and even more so for RBF (Table 2). Similar to what was observed in the data presented in this work, Anderson, Thompson, and Austin (2005), Liu et al. (2007), and Asal (2016) observed an asymptotic tendency of RMSE to d100 RMSE as point cloud density increases (Figure 4), but they reported a homogeneous RMSE group from d100 to d50, which does not agree with our results.

The reported elevation accuracies of DSMs generated from UAV photogrammetry and SfM and MSV techniques are 3.1 cm (Cryderman, Bill Mah, and Shufletoski 2014), 4 cm (Oniga, Breaban, and Statescu 2018), 4.7 cm (Agüera-Vega, Carvajal-Ramírez, and Martínez-Carricondo 2017), and 6.62 cm (Uysal, Toprak, and Polat 2015), but none of these indicate the part of the error attributable to the DSM generation process, which may be needed to define methodologies to maximize the accuracy of the DSM.

5. Conclusions

UAV-photogrammetry based on SfM and MSV offers high-accuracy and high-density 3D point clouds for detailed representation of terrain surfaces. Very high-density data can entail redundant information, however, and long processing times may therefore be needed to generate the DSM. Furthermore, knowledge of how each factor involved in the generation of the DSM influences the error associated with it could help develop methodologies to minimize this error.

This work studied how the 3D point cloud density and the interpolation method affect DSM accuracy for data acquired from UAV and using SfM and MSV techniques.

The main conclusions derived from the results of this work are as follows:

- Point cloud density, GS, and interpolation method significantly affect DSM accuracy.
- Although differences in accuracy between IDW, KR, and TLI are not very high, IDW showed lower RMSE values. MRBF yielded the worse accuracies.
- The higher the point density, the greater the accuracy of the DSM. For the IDW interpolator, the RMSE for the 3D point cloud generated from UAV-photogrammetry software including SfM and MVS techniques was 1.054 cm. The RMSE increased by 3% when a point cloud with 80% extracted from the raw cloud was used to generate the DSM. When the point cloud included 40% of the raw cloud, RMSE increased by 5%. For densities lower than 15%, RMSE increased exponentially (45% for 1% of raw cloud).

- The GS that minimized the RMSE for densities of 20% or higher was 1 cm, which represents two times the GSD of the pictures used for developing the photogrammetry project.
- The results of this study show the possibility of stablishing empirical relationships between the expected RMSE in the interpolation of a grid DSM and such variables as point cloud density, GS, and even interpolator used. For example, the observed relationship between RMSE and point cloud density is adjusted with remarkable approximation to a decreasing potential. Similarly, relationship between RMSE and GS shows a remarkable approximation to a parabolic function. Therefore, to generate a DSM with a given RMSE, it could be possible to stablish the appropriate GS and/or point cloud density for a particular interpolator, with the economy in computing time and file size.
- Further analysis is needed to check the generalizations of the conclusions, such as different surface morphologies, GSD, and even interpolation variant (e.g. power different from 2 in the IDW interpolator).

Declaracion of interst statement

The authors declare that they have no known competing financial interests or personal relationships that could have appeared to influence the work reported in this paper.

Disclosure statement

No potential conflict of interest was reported by the authors.

ORCID

F. Agüera-Vega ⓘ http://orcid.org/0000-0003-0709-3388
P. Martínez-Carricondo ⓘ http://orcid.org/0000-0001-9556-7998
F. Carvajal ⓘ http://orcid.org/0000-0001-7791-0991

References

Agüera Vega, F., F. C. Ramírez, M. P. Saiz, and F. O. Rosúa. 2015. "Multi-Temporal Imaging Using an Unmanned Aerial Vehicle for Monitoring a Sunflower Crop." *Biosystems Engineering* 132. doi:10.1016/j.biosystemseng.2015.01.008.

Agüera-Vega, F., F. Carvajal-Ramírez, and P. Martínez-Carricondo. 2017. "Accuracy of Digital Surface Models and Orthophotos Derived from Unmanned Aerial Vehicle Photogrammetry." *Journal of Surveying Engineering* 143 (2): 04016025. doi:10.1061/(ASCE)SU.1943-5428.0000206.

Agüera-Vega, F., F. Carvajal-Ramírez, P. Martínez-Carricondo, J. S.-H. López, F. J. Mesas-Carrascosa, A. García-Ferrer, and F. J. Pérez-Porras. 2018. "Reconstruction of Extreme Topography from UAV Structure from Motion Photogrammetry." *Measurement: Journal of the International Measurement Confederation* 121 (February): 127–138. doi:10.1016/j.measurement.2018.02.062.

Anderson, E. S., J. A. Thompson, and R. E. Austin. 2005. "LIDAR Density and Linear Interpolator Effects on Elevation Estimates." *International Journal of Remote Sensing* 26 (18): 3889–3900. doi:10.1080/01431160500181671.

Asal, F. F. 2016. "Evaluating the Effects of Reductions in LiDAR Data on the Visual and Statistical Characteristics of the Created Digital Elevation Models." *ISPRS Annals of the Photogrammetry, Remote Sensing and Spatial Information Sciences* 3 (July): 91–98. doi:10.5194/isprs-annals-III-2-91-2016.

Asensio, C., J. Weber, F. Lozano, and L. Mielnik. 2019. "Laser-Scanner Used in a Wind Tunnel to Quantify Soil Erosion." *International Agrophysics* 33 (2): 227–232. doi:10.31545/intagr/109424.

Atkinson, K. B. 1996. *Close Range Photogrammetry and Machine Vision*. Whitttles Publishing, London.

Brown, D. C. 1971. "Close-Range Camera Calibration." *Photogrammetric Engineering and Remote Sensing* 8: 855–866.

Campos, J., J. Llop, M. Gallart, F. García-Ruiz, A. Gras, R. Salcedo, and E. Gil. 2019. "Development of Canopy Vigour Maps Using UAV for Site-Specific Management during Vineyard Spraying Process." *Precision Agriculture* 20 (123456789): 1136–1156. doi:10.1007/s11119-019-09643-z.

Carlson, R. E., and T. A. Foley. 1991. "The Parameter R2 in Multiquadric Interpolation." *Computers and Mathematics with Applications* 21 (9): 29–42. doi:10.1016/0898-1221(91)90123-L.

Carlson, R. E., and T. A. Foley. 1992. "Interpolation of Track Data with Radial Basis Methods." *Computers and Mathematics with Applications* 24 (12): 27–34. doi:10.1016/0898-1221(92)90169-I.

Carrivick, J. L., M. W. Smith, and D. J. Quincey. 2016. *Structure from Motion in the Geosciences*. John Wiley & Sons. Oxford, UK. doi:10.1002/9781118895818.

Castillo, C., R. Pérez, M. R. James, J. N. Quinton, E. V. Taguas, and J. A. Gómez. 2012. "Comparing the Accuracy of Several Field Methods for Measuring Gully Erosion." *Soil Science Society of America Journal* 76 (4): 1319–1332. doi:10.2136/sssaj2011.0390.

Cryderman, C., S. Bill Mah, and A. Shufletoski. 2014. "Evaluation of UAV Photogrammetric Accuracy for Mapping and Earthworks Computations." *GEOMATICA* 68 (4): 309–317. doi:10.5623/cig2014-405.

Eltner, A., A. Kaiser, C. Castillo, G. Rock, F. Neugirg, and A. Abellan. 2015. "Image-Based Surface Reconstruction in Geomorphometry – Merits, Limits and Developments of a Promising Tool for Geoscientists." *Earth Surface Dynamics Discussions* 3 (4): 1445–1508. doi:10.5194/esurfd-3-1445-2015.

Franke, R. 1982. "Scattered Data Interpolation: Test of Some Methods." *Mathematics of Computations* 33 (157): 181–200.

García-Serrana, M., J. S. Gulliver, and J. L. Nieber. 2018. "Description of Soil Micro-Topography and Fractional Wetted Area under Runoff Using Fractal Dimensions." *Earth Surface Processes and Landforms* 43 (13): 2685–2697. doi:10.1002/esp.4424.

Gašparovic, M., and D. Gajski. 2016. "Two-Step Camera Calibration Method Developed for Micro UAV'S." *International Archives of the Photogrammetry, Remote Sensing and Spatial Information Sciences - ISPRS Archives* 2016 (Janua (July)): 829–833. doi:10.5194/isprsarchives-XLI-B1-829-2016.

Golden Software. 2019. https://www.goldensoftware.com/products/surfer

Gong, C., S. Lei, Z. Bian, Y. Liu, Z. Zhang, and W. Cheng. 2019. "Analysis of the Development of an Erosion Gully in an Open-Pit Coal Mine Dump during a Winter Freeze-Thaw Cycle by Using Low-Cost UAVs." *Remote Sensing* 11 (11): 1356. doi:10.3390/rs11111356.

Hartley, R., and A. Zisserman. 2003. "Multiple View Geometry." *Journal of Chemical Information and Modeling*. Vol. 53. doi:10.1017/CBO9781107415324.004.

Hengl, T. 2006. "Finding the Right Pixel Size." *Computers & Geosciences* 32 (9): 1283–1298. doi:10.1016/j.cageo.2005.11.008.

Jaud, M., S. Passot, R. Le Bivic, C. Delacourt, P. Grandjean, and N. Le Dantec. 2016. "Assessing the Accuracy of High Resolution Digital Surface Models Computed by PhotoScan® and MicMac® in Sub-Optimal Survey Conditions." *Remote Sensing* 8 (6): 465. doi:10.3390/rs8060465.

Juan, L., and O. Gwun. 2009. "A Comparison of Sift, Pca-Sift and Surf." *International Journal of Image Processing (IJIP)* 3 (4): 143–152. doi:10.1007/s11270-006-2859-8.

Lee, D. T., and B. J. Schachter. 1980. "Two Algorithms for Constructing a Delaunay Triangulation." *International Journal of Computer & Information Sciences* 9 (3): 219–242. doi:10.1007/BF00977785.

Liu, X., and Z. Zhang. 2008. "Lidar Data Reduction for Efficient and High Quality Dem Generation." *The International Archives of the Photogrammetry, Remote Sensing and Spatial Information Sciences* XXXVII (Part B3b): 173–178.

Liu, X., Z. Zhang, J. Peterson, and S. Chandra. 2007. "The Effect of LiDAR Data Density on DEM Accuracy." *International Congress on Modelling and Simulation (MODSIM07)* 1363–1369. http://eprints.usq.edu.au/3781

Lloyd, C. D., and P. M. Atkinson. 2002. "Deriving DSMs from LiDAR Data with Kriging." *International Journal of Remote Sensing* 23 (12): 2519–2524. doi:10.1080/01431160110097998.

Luhmann, T., C. Fraser, and H. G. Maas. 2016. "Sensor Modelling and Camera Calibration for Close-Range Photogrammetry." *ISPRS Journal of Photogrammetry and Remote Sensing* 115: 37–46. doi:10.1016/j.isprsjprs.2015.10.006.

Mancini, F., M. Dubbini, M. Gattelli, F. Stecchi, S. Fabbri, and G. Gabbianelli. 2013. "Using Unmanned Aerial Vehicles (UAV) for High-Resolution Reconstruction of Topography: The Structure from Motion Approach on Coastal Environments." *Remote Sensing* 5 (12): 6880–6898. doi:10.3390/rs5126880.

Martinez-Guanter, J., P. Agüera, J. Agüera, and P.-R. Manuel. 2019. "Spray and Economics Assessment of a UAV-Based Ultra-Low-Volume Application in Olive and Citrus Orchards". *Precision Agriculture* (123456789). doi:10.1007/s11119-019-09665-7.

Metashape, A. 2019. No Title. https://www.agisoft.com/

Momm, H. G., R. L. Bingner, R. R. Wells, S. M. Dabney, and L. D. Frees. 2013. "Effect of Terrestrial LiDAR Point Sampling Density in Ephemeral Gully Characterization." *Open Journal of Modern Hydrology* 3 (1): 38–49. doi:10.4236/ojmh.2013.31006.

Nesbit, P. R., and C. H. Hugenholtz. 2019. "Enhancing UAV-SfM 3D Model Accuracy in High-Relief Landscapes by Incorporating Oblique Images." *Remote Sensing* 11 (3): 1–24. doi:10.3390/rs11030239.

Nex, F., and F. Remondino. 2014. "UAV for 3D Mapping Applications: A Review." *Applied Geomatics* 6 (1): 1–15. doi:10.1007/s12518-013-0120-x.

Oniga, V.-E., A.-I. Breaban, and F. Statescu. 2018. "Determining the Optimum Number of Ground Control Points for Obtaining High Precision Results Based on UAS Images." *Proceedings* 2 (7): 7. doi:10.3390/ecrs-2-05165.

Pérez, M., F. Agüera, and F. Carvajal. 2013. "Low Cost Surveying Using an Unmanned Aerial Vehicle." In *International Archives of the Photogrammetry, Remote Sensing and Spatial Information Sciences - ISPRS Archives*. Editors: G. Grenzdörffer and R. Bill. Vol. 40, 311-315.

Pix4Dmapper. 2019. No Title. https://www.pix4d.com/product/pix4dmapper-Photogrammetry-Software

Powell, M. J. D. 1990. *The Theory of Radial Basis Function Approximation in 1990*. Vol. 12, 105–209. University of Cambridge, Department of Applied Mathematics and Theoretical Physics. Cambridge.

Remondino, F., and C. Fraser. 2006. "Digital Camera Calibration Methods: Considerations and Comparisons." *International Archives of Photogrammetry, Remote Sensing and Spatial Information Sciences* 36 (5): 266–272.

Remondino, F., and S. El-Hakim. 2006. "Image-Based 3D Modelling: A Review." *The Photogrammetric Record* 21 (115): 269–291. doi:10.1111/j.1477-9730.2006.00383.x.

Rossi, G., L. Tanteri, V. Tofani, P. Vannocci, S. Moretti, and N. Casagli. 2018. "Multitemporal UAV Surveys for Landslide Mapping and Characterization." *Landslides* 15 (5): 1045–1052. doi:10.1007/s10346-018-0978-0.

Schmid, T., H. Schack-Kirchner, and E. Hildebrand. 2014. "A Case Study of Terrestrial Laser Scanning in Erosion Research: Calculation of Roughness and Volume Balance at A Logged Forest Site." *International Archives of Photogrammetry, Remote Sensing and Spatial Information Sciences* XXXVI (8): 114–118.

Schwendel, A. C., and D. J. Milan. 2019. "Terrestrial Structure-from-Motion: Spatial Error Analysis of Roughness and Morphology." *Geomorphology* 127065. doi:10.1016/j.geomorph.2019.106883.

Singh, K. K., G. Chen, J. B. McCarter, and R. K. Meentemeyer. 2015. "Effects of LiDAR Point Density and Landscape Context on Estimates of Urban Forest Biomass." *ISPRS Journal of Photogrammetry and Remote Sensing* 101: 310–322. doi:10.1016/j.isprsjprs.2014.12.021.

Smith, M. W., and J. Warburton. 2018. "Microtopography of Bare Peat: A Conceptual Model and Objective Classification from High-Resolution Topographic Survey Data." *Earth Surface Processes and Landforms*. Vol. 43. doi:10.1002/esp.4336.

Snavely, N., S. M. Seitz, and R. Szeliski. 2008. "Modeling the World from Internet Photo Collections." *International Journal of Computer Vision* 80 (2): 189–210. doi:10.1007/s11263-007-0107-3.

UgCS. 2019. Https://www.ugcs.com/

Uysal, M., A. S. Toprak, and N. Polat. 2015. "DEM Generation with UAV Photogrammetry and Accuracy Analysis in Sahitler Hill." *Measurement: Journal of the International Measurement Confederation* 73: 539–543. doi:10.1016/j.measurement.2015.06.010.

Vasuki, Y., E.-J. Holden, P. Kovesi, and S. Micklethwaite. 2014. "Semi-Automatic Mapping of Geological Structures Using UAV-Based Photogrammetric Data: An Image Analysis Approach." *Computers & Geosciences* 69 (August): 22–32. doi:10.1016/j.cageo.2014.04.012.

Westoby, M. J., J. Brasington, N. F. Glasser, M. J. Hambrey, and J. M. Reynolds. 2012. "Structure-from-Motion? Photogrammetry: A Low-Cost, Effective Tool for Geoscience Applications." *Geomorphology* 179 (December): 300–314. doi:10.1016/j.geomorph.2012.08.021.

Yang, X., and T. Hodler. 2000. "Visual and Statistical Comparisons of Surface Modeling Techniques for Point-Based Environmental Data." *Cartography and Geographic Information Science* 27 (2): 165–176. doi:10.1559/152304000783547911.